


Fluorine-free gel polymer electrolyte for lithium oxide-rich solid electrolyte interphase and stable Li metal batteries

Received: 18 December 2024

Accepted: 9 September 2025

Published online: 21 October 2025

 Check for updatesWeijian Xu¹, Lingxi Zhou², Songxin Lu¹, Jiahui He¹, Yongbin Xu¹ & Lei Tian¹  

The development of stable solid-electrolyte interphases (SEI) represents a fundamental challenge for Li-metal batteries. Although fluorinated reagents improve cycling performance through LiF-rich SEI formation, their associated costs and environmental impacts remain problematic. Here, we present a fluorine-free quasi-solid polymer electrolyte that generates an O/N-containing hybrid SEI with improved interfacial stability and Li⁺ transport kinetics. This unique SEI architecture preferentially directs Li deposition along the (200) crystallographic plane while enhancing charge-transfer efficiency. When implemented in Li | LiNi_{0.8}Co_{0.1}Mn_{0.1}O₂ full cells, the fluorine-free gel polymer electrolyte enables a capacity retention of 84.7% over 800 cycles at 3 C. The fluorine-free gel polymer electrolyte system reported here exhibits improved high-rate performance compared to conventional fluorinated polymer electrolytes, providing a sustainable materials design paradigm for next-generation solid-state batteries.

With the rapid development of high technologies such as electric aviation, deep space exploration and deep-sea underwater vehicles, the demand for energy systems with high energy density is rising^{1,2}. To achieve a secondary battery with satisfactory performance, it is crucial to construct a robust solid electrolyte interface (SEI)^{3,4}. The oxidation-reduction potential of Li metal is usually lower than the electrochemical window of the electrolyte, allowing the electrolyte to form the corresponding SEI on the surface of the Li metal during the first charge/discharge⁵. SEI exhibits both ionic conductivity and electronic insulation properties, which can effectively prevent the co-embedding of solvent molecules and avoid the damage of electrode materials, thus improving the cycling performance and service life of electrodes^{6,7}.

Typical SEI components, such as Li oxide (Li₂O), Li nitride (Li₃N) and Li fluoride (LiF), possess good electrochemical stability and high interfacial energy with Li metal, which is conducive to the diffusion of Li ions^{8–11}. At the same time, they also have decent mechanical properties and play a crucial role in inhibiting the growth of Li dendrites¹². Moreover, the composition of SEI can affect the deposition morphology and sediment-stripping reversibility of the surface of Li metal

crystals, which largely determines the periodic performance of batteries¹³. Currently, extensive research efforts are dedicated to enhancing battery performance by increasing the fluorine content, attributed to its ability to form stable LiF^{14,15}. However, the use of large amounts of fluorine-containing additives and solvents raises concerns about high costs and environmental pollution hazards, further limiting their widespread application^{16–18}. Therefore, there is an urgent need to develop high-performance secondary batteries based on a fluorine-free design concept.

In response to this emerging idea of fluorine-free, researchers have conducted a series of studies focusing on reducing fluorine content, using fluorine-free solvents, or designing some fluorine-free additives to replace fluoro-ethers. Song et al. introduced an asymmetric amphiphilic ether (MNBE) as a co-solvent in the Li bis(fluorosulfonyl)imide (LiFSI)/ dimethoxyethane (DME) electrolyte system¹⁹. This fluorine-free micelle-like solvated electrolyte can promote the decomposition of more FSI on the Li metal surface, thereby forming an SEI rich in LiF. Furthermore, Wang et al.²⁰ designed a methylated ether electrolyte, a fluorine-free solvent that can control anion formation and improve oxidation stability, forming an interface phase rich in LiF, which can

¹College of Chemistry and Environmental Engineering, Shenzhen University, Shenzhen, P. R. China. ²School of Materials Science and Engineering, Tsinghua University, Beijing, P. R. China. ✉ e-mail: leitian@szu.edu.cn

inhibit the formation of Li dendrites and reduce negative electrode fragmentation at high voltages. Notably, Zhu et al.²¹ successfully developed a low-fluorine diluted electrolyte (1,3-DIOX) for 4.5 V high-voltage Li metal batteries through a salt engineering strategy. However, previous research has predominantly centered on the construction of fluorinated interfaces. Currently emerging fluorine-free polymer electrolyte systems mainly employ borate salts, with traditional matrices like Poly(methyl methacrylate) (PMMA)^{22,23}, poly ethylene oxide (PEO)²⁴, or nano-composite PMMA-based electrolytes²⁵ as the primary components. Unfortunately, the relatively narrow electrochemical window of these systems severely restricts their compatibility with high-voltage positive electrode. Moreover, there has been a lack of in-depth research on the composition and structure of the SEI, resulting in poor cycling performance of the batteries. This undoubtedly hinders their further development and application. In view of this, it is particularly urgent to develop a current type of fluorine-free polymer electrolyte with high interfacial compatibility through molecular structure design and interface engineering optimization, construct a fluorine-free SEI with controllable composition, and deeply analyze its structure-performance relationship. An ideal fluorine-free polymer electrolyte should exhibit the following essential characteristics: (1) Favorable ionic conductivity to ensure rapid Li ion transport²⁶; (2) The ability to form a solvent-rich structure with the fluorine-free anion to produce a stable inorganic-rich SEI²⁷; (3) Good cycling stability when utilized in conjunction with high nickel and high-voltage positive electrode²⁸. Despite the encouraging progress made in optimizing electrolyte compositions for Li metal batteries²⁹, the achievement of SEI with fully fluorine-free to attain highly stable Li metal batteries has yet to be addressed.

Here, we report a sustainable fluorine-free SEI design based on a quasi-solid polymer electrolyte (PVM-GPE) that is rich in Li₂O inorganic components, enabling respectable stability in interface properties. The PVM-GPE not only exhibits a satisfactory ionic conductivity (1.4×10^{-3} S cm⁻¹), but also demonstrates a high ionic migration number (0.77). The formed fluorine-free SEI effectively regulates the uniform deposition of Li metal along the surface of the (200) crystal rather than the formation of Li dendrites, thereby improving the interfacial migration dynamics of Li ions. Quantitative analysis of oxygen content in SEI shows that a high Li₂O content corresponds to a long-term stable cycle of the battery. In particular, Li||Li and Li||Cu cells containing PVM-GPE exhibit high electroplating/stripping stability. In addition, the Li|PVM-GPE|NCM811 battery maintains acceptable capacity at high rate and high voltage. The proposed fluorine-free SEI strategy provides a modern design concept for manufacturing high-performance solid-state batteries.

Results and discussion

Molecular design concepts for fluorine-free polymer electrolytes

Through in situ radical copolymerization, we successfully synthesized a fluorine-free polymer electrolyte (PVM-GPE). The resulting SEI layer primarily consists of Li₂O/Li₃N (Fig. 1a), which not only stabilises the negative electrode of Li metal and improves the cycle-life performance of the battery, but also signifies a prominent direction for sustainable development in the field of polymer solid-state electrolytes. Highly polar cyclic vinyl carbonate (VC) acts as the main ion-conducting segment of the polymer matrix owing to its high binding energy with Li⁺. While N, N'-methylenebisacrylamide (MBA) serves as a cross-linking agent to promote better mechanical properties between the polymer chains and via hydrogen bonding interactions as an anionic anchoring site, contributing to a higher Li⁺ transfer in PVM-GPE. More considerably, the presence of strongly polar VC and weakly polar MBA enables the presence of weak solvation of Li⁺, thus ensuring the Li⁺ migration process. The carbonyl oxygen on PVM-GPE exhibits a stronger binding energy to Li⁺ (Fig. 1b and Supplementary Data 1), indicating a preferential coordination of Li⁺ to this site. Nevertheless,

the weak binding energy of Li⁺ with MBA can be attributed to the electronegativity of nitrogen, which reduces the electron cloud density in carbonyl oxygen (Fig. 1c and Supplementary Data 1).

Furthermore, we simulated the molecular orbitals of each molecule by quantum chemistry (Fig. 1d and Supplementary Data 1). The outcome implies that the Lowest Unoccupied Molecular Orbital (LUMO) energy value of the polymerised PVM-GPE is lower than that of VC and MBA. Hence, it is able to preferentially reduce on the Li metal surface to form N- and O-rich SEI. In the meantime, VC has the lowest Highest Occupied Molecular Orbital (HOMO) energy value, which is expected to enhance the oxidative stability of the PVM-GPE molecular chain. The introduction of nitride functional groups in the high-speed conduction ionic segment VC facilitates the formation of N- and O-rich SEI and induces the uniform deposition of Li ions (Li⁺). Meanwhile, the network structure of B- and N-rich positive electrode electrolyte interface (CEI) and polymer cross-linking effectively mitigates the cracking of the high-Ni positive electrode. Compared with the current mainstream polymer electrolytes, the as-developed PVM-GPE stands out for comparable stability in high-rate cycling (Fig. 1e, Supplementary Table 1)^{30–39}.

We selected the mixture of propylene carbonate (PC) and DME as the base liquid electrolyte due to their combined advantages in electrochemical performance and interfacial stability^{40,41}. While choosing Li nitrate (LiNO₃) as an interfacial film-forming additive and LiBOB as the Li salt to enhance the cycling stability and rate performance of the battery under high-voltage conditions, leveraging their synergistic effects in improving battery performance^{42,43}. Therefore, in this study, we composed a liquid electrolyte by adding 1 mol L⁻¹ of LiBOB and 0.2 mol L⁻¹ of LiNO₃ to PC:DME mixture with a volume ratio of 1:3 (PDE). The comparison sample for PVM-GPE is the PDE electrolyte used in the precursor solution to spotlight the dominance of the fluoropolymer-free molecule PVM-GPE. We experimentally verified this guideline. Fourier transform infrared spectroscopy (FT-IR) is used to characterize the molecular structure of the polymer. (Supplementary Fig. 1) demonstrates that both the HN-C=O group on MBA and the C=O group on VC occur in PVM. The C=C double bond in Polymer molecules copolymerized from VC and MBA disappears, indicating that PVM can successfully polymerize. Optical photographs after polymerisation also indicate the capacity to solidify to form a gel electrolyte (Supplementary Fig. 2). As shown in Supplementary Fig. 3, the thermal properties of the electrolyte were analyzed using thermogravimetric analysis (TGA). PVM-GPE experiences a 10% weight loss at around 167 °C, which is attributed to the evaporation of solvents. Meanwhile, PVM molecules exhibit a 5% mass loss at 300 °C, collectively confirming its good thermal stability. Furthermore, according to the differential scanning calorimetry (DSC) plot presented in Supplementary Fig. 4, PVM-GPE exhibits a low glass transition temperature (T_g) of -34 °C, indicating rapid segmental dynamics within the polymer network and high ionic conductivity⁴⁴.

The solvation structure of the PVM-GPE in the electrolyte plays a crucial role in the formation of SEI. To understand whether the PVM-GPE can effectively regulate the solvation behaviour of the electrolyte, we used molecular dynamics (MD) to simulate the electrolyte environment (Supplementary Data 1). Figure 2a, b demonstrates the simulated snapshots and local zoomed-in comparison plots of PVM-GPE and PDE electrolytes. The figure clearly demonstrates that PVM-GPE successfully participates in the formation of Li⁺ solvated sheath structure. The coordination number (CN) and radial distribution function (RDF) of the different electrolytes are shown in Fig. 2c, d. The RDF of oxygen atoms in the solvent and anions was calculated to quantify the local environment around Li⁺. The analysis demonstrates that the main solvation structure in PDE electrolyte is influenced by the interaction between Li⁺ and solvent molecules, with a coordination number of 3.3 for Li⁺ with solvent molecules, indicating that Li⁺ is coordinated with three solvent molecules. In contrast, in the PVM-GPE

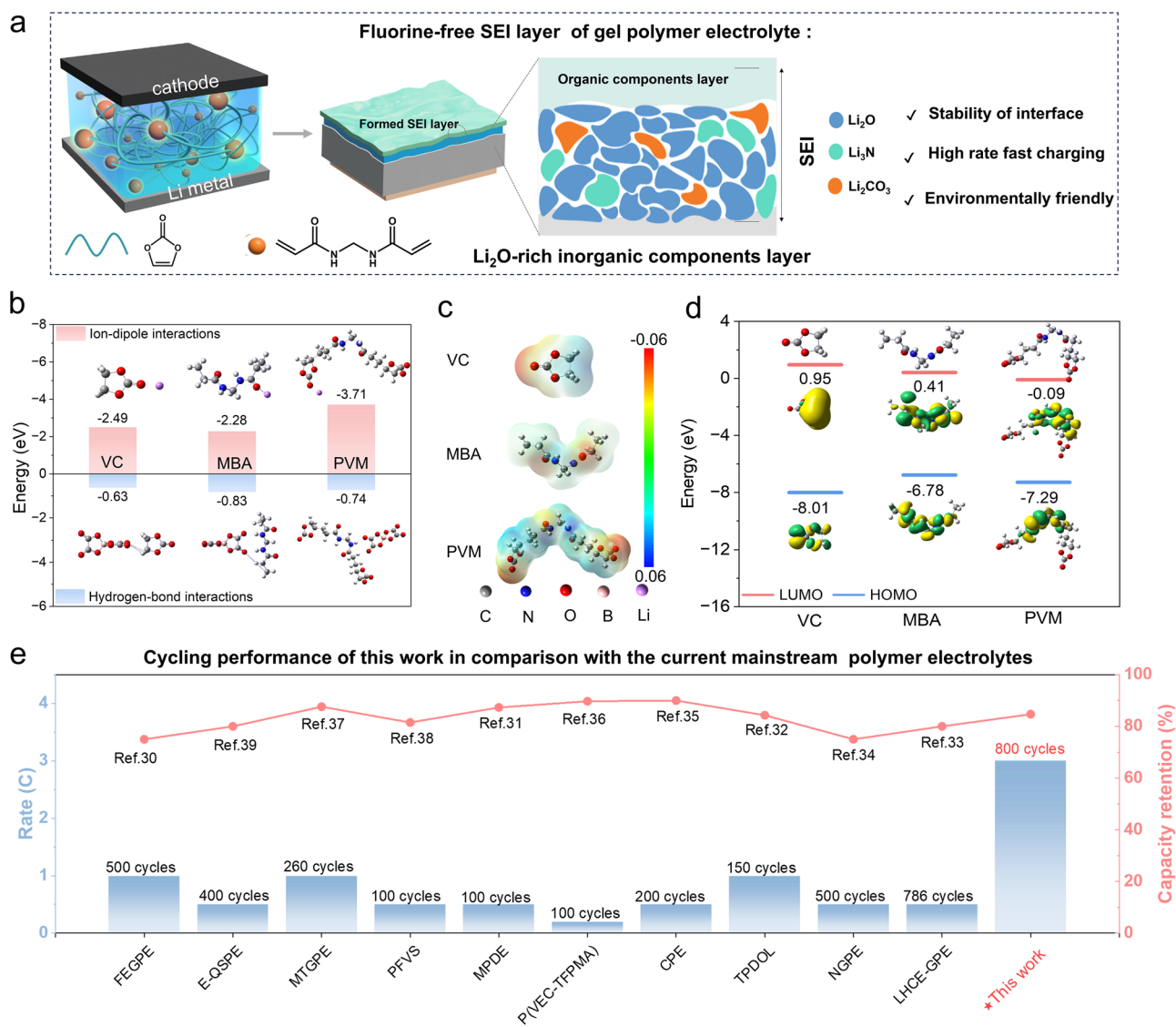


Fig. 1 | Sustainable fluorine-free polymer solid electrolyte interface. a Fluorine-free SEI layer design for solid polymer electrolyte. **b** Density Functional Theory (DFT) calculations of the binding energies of Li ions and anionic BOB⁻ with VC, MBA and PVM-GPE respectively. **c** Electrostatic potential (ESP) graphs for VC, MBA and

PVM-GPE. **d** LUMO and HOMO energy diagrams for VC, MBA and PVM-GPE and their optimised structures. **e** Cycling performance of this work in comparison with the current mainstream polymer electrolytes.

system, distinct sharp peaks were observed in the RDF at 2.07, 2.04, 2.03, and 2.14 Å with varying intensities, indicating that BOB⁻, PC, and PVM primarily constitute the Li⁺ solvation sheath in this system. Notably, the BOB⁻ dominates the solvation shell, forming an anion-dominated solvation structure. In particular, beyond solvation by solvent molecules and anions, Li⁺ further engages in coordination with PVM. The CN of Li⁺ with PVM reaches 1.68, while the CN of solvent molecules decreases. This suggests that PVM facilitates the expulsion of solvent molecules, thereby promoting the formation of an anion-rich solvation structure. The expected coordinated solvation structures of Li⁺ in PVM-GPE and PDE, obtained from MD simulations, are shown in Supplementary Fig. 5. Stable interaction networks are formed between PVM chain segments and solvent molecules and ions. This solvation structure aids in maintaining the ionic conductivity of the electrolyte and facilitates ion transport. Compared to the PDE system, the solvation energy of PVM-GPE is -10.12 eV, indicating that the solvation energy formed in the PVM-GPE system is relatively low. This facilitates the desolvation process and hopping conduction of Li⁺, thus enabling rapid migration⁴⁵. To further verify the existence of the solvated structure in the PVM-GPE, we conducted Raman spectroscopy

analysis. As illustrated in Supplementary Fig. 6, we utilized Raman spectroscopy to probe the solvation structures within various electrolyte systems. In the PDE system, the solvation structure is predominantly characterized by aggregates (AGGs), accounting for 53.8% of the total, which is consistent with the solvation structure observed in MD simulations. However, in the PVM system, the proportion of AGGs structures decreases (accounting for 35.9%), as evidenced by the coordination number of Li⁺ with BOB⁻. The molecular structure of the polymer matrix is also incorporated into the solvation structure, occupying a certain steric space within it. This steric hindrance effect weakens the coordination interaction between BOB⁻ and Li⁺⁴⁶. Consequently, the original AGGs structures are disrupted and transformed into contact ion pairs (CIPs) with direct Li⁺-BOB⁻ binding (accounting for 50.4%)^{47,48}. This transformation reduces the confinement of Li⁺ by PVM and promotes Li⁺ migration.

Furthermore, the diffusion rate of Li⁺ in different electrolytes can be assessed by mean square displacement (MSD) (Supplementary Fig. 7). It revealed that the diffusion coefficient of PVM-GPE is slightly reduced, suggesting that the formation of a modified coordination structure between Li⁺ and PVM-GPE contributes to the Li⁺

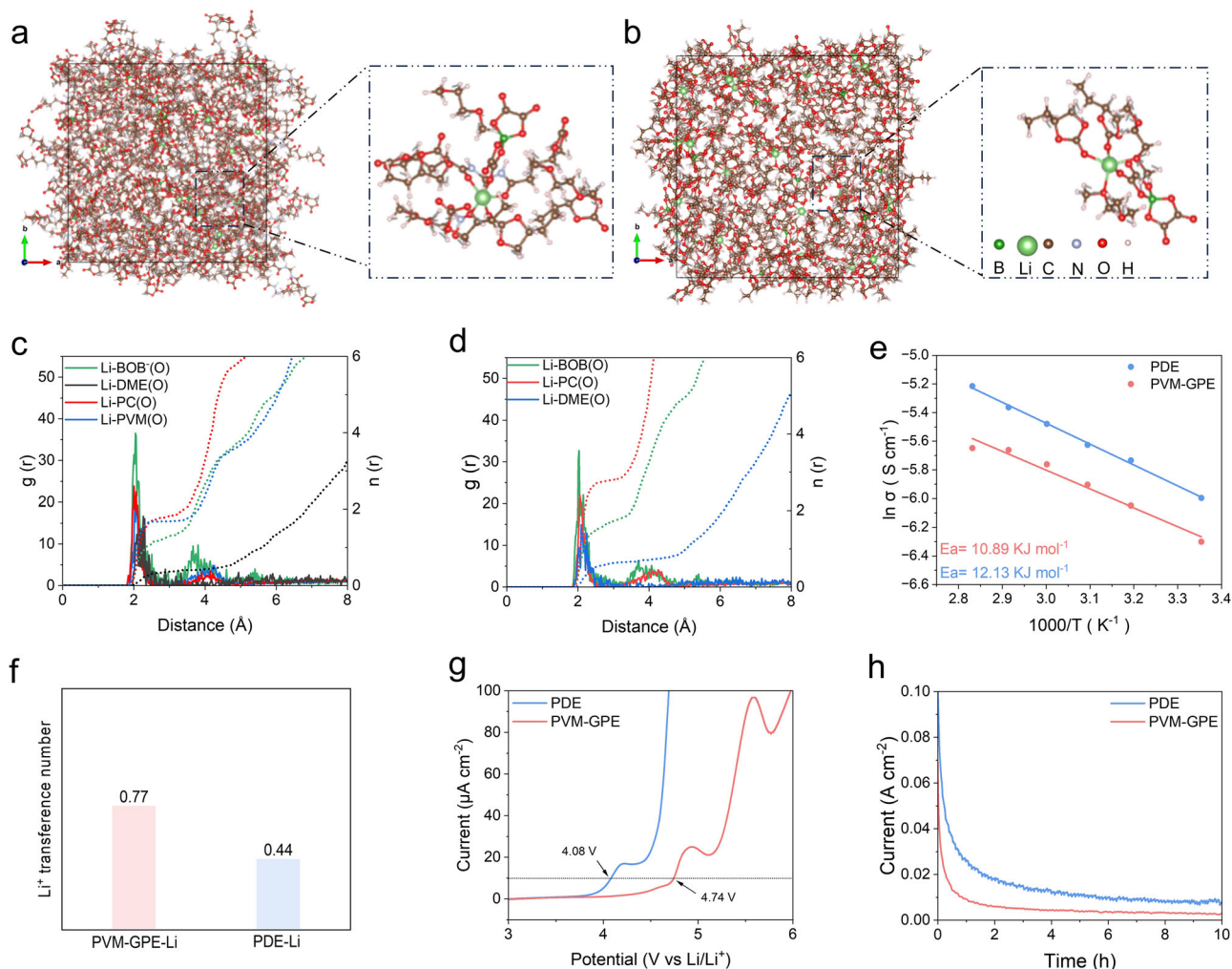


Fig. 2 | Exploration of the kinetics of Li⁺ transport by electrolytes. Local magnification of solvation simulation snapshots and radial distribution function (RDF) and coordination number (CN) of PVM-GPE (**a, c**) and PDE (**b, d**). **e** Arrhenius of ionic conductivity of different electrolytes. **f** Li⁺ transfer number of PVM-GPE and PDE at 25°C. **g** Linear scanning voltammetry (LSV) curves of PVM-GPE and PDE at 25°C. **h** Li | |NCM811 leakage current test at 4.5 V constant voltage.

microdynamics⁴⁹. PVM-GPE maintains a weakly interacting solvated structure and improves the interfacial stability between the electrolyte and Li metal through anion-derived SEI. Electrochemical impedance (EIS) is tested at different temperatures to investigate the ionic conductivity of the PVM-GPE (Supplementary Fig. 8). As the temperature increases, the impedance of PVM-GPE and PDE electrolytes gradually decreases. The ionic conductivities of the PVM-GPE and PDE electrolytes are $1.4 \times 10^{-3} \text{ S cm}^{-1}$ and $2.0 \times 10^{-3} \text{ S cm}^{-1}$ at 25°C, respectively. Such ionic conductivity is sufficient to ensure favorable rate performance for quasi-solid-state Li metal batteries.

The correspondence between ionic conductivity and temperature is shown in the Arrhenius curve of Fig. 2e. The activation energy of PVM-GPE ($10.89 \text{ kJ mol}^{-1}$) is lower than that of PDE ($12.13 \text{ kJ mol}^{-1}$), which suggests that there is a lower transport energy barrier for Li⁺ in PVM-GPE³⁵. High Li ion migration number (t_{Li^+}) serves as a crucial metric for evaluating the efficacy of ion transport. An accurate calculation of this parameter is achieved through the application of the Bruce-Vincent equation. As illustrated in Fig. 2f and Supplementary Fig. 9, PVM-GPE demonstrates the highest ion transport number of 0.77. We conducted DFT calculations to investigate the transport mechanism of Li⁺ (Supplementary Fig. 10 and Supplementary Data 1). The findings suggest that the binding energy of the PVM-Li complex is lower than that of the BOB-Li complex, suggesting that the anion forms a tightly bound ion pair with Li⁺, which obstructs the migration of Li⁺.

However, the binding energy between PVM (-3.71 eV) and Li⁺ is higher than that with PC (-2.55 eV) and DME (-1.98 eV). Thus, the presence of PVM imparts a certain “dragging” capability, thereby reducing the binding of the anion to Li⁺ and increasing the t_{Li^+} ⁵⁰. We discovered that the C-H bonds on PVM, acting as positive dipoles, can form ion-dipole interactions with the BOB⁻ anion. The affinity resulting from these interactions is higher than that PC and DME, restricting the mobility of the anion and further enhancing the t_{Li^+} ⁵¹. Subsequently, we analyzed the contribution of Li⁺ to the ionic conductivity and deduced that PVM-GPE exhibits higher Li-ion conductivity (Supplementary Fig. 11), which corresponds to its performance in high-speed, long-cycle operations. The electrochemical stability window of the electrolyte system was investigated using Linear Scan Voltammetry (LSV). As shown in Fig. 2g and Supplementary Fig. 12, the current of PVM-GPE begins to increase at a voltage of 4.74 V, indicating its high oxidation stability, which is reliable to that of traditional PDE electrolytes. Subsequently, a leakage current test was conducted at a constant voltage of 4.5 V (Fig. 2h). The battery utilizing PVM-GPE exhibited a smaller leakage current at this constant voltage of 4.5 V, suggesting its satisfactory stability and consequently good electrochemical performance⁵².

Structure and components characterization of SEI

The electrolyte solvation layer structure directly determines the chemical composition of the SEI and these compositions determine the

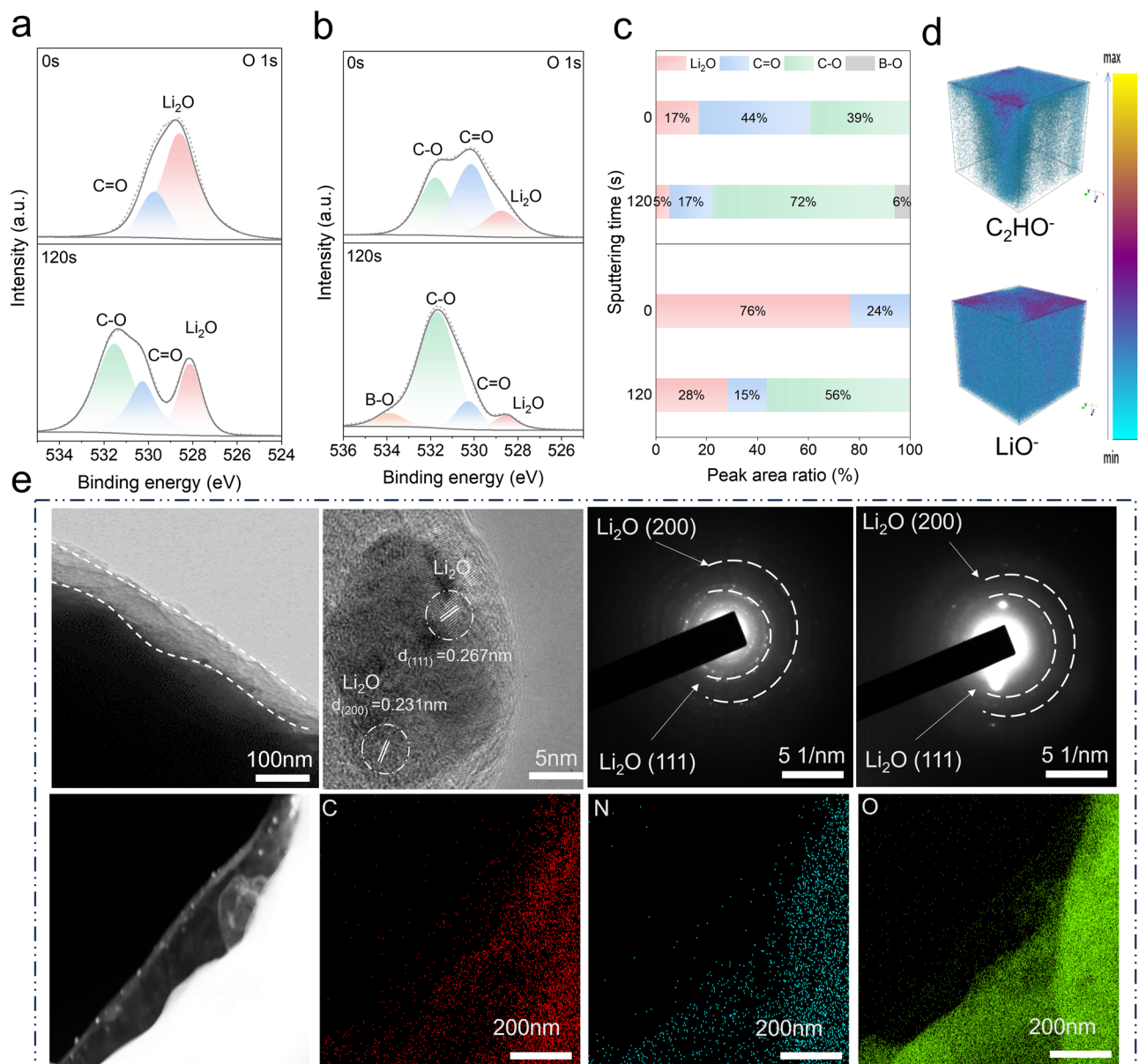


Fig. 3 | A fluorine-free SEI layer dominated by Li₂O. **a, b** XPS depth analysis of O 1s for the SEI layer of (a) PVM-GPE and (b) PDE electrolyte. **c** Comparison of peak area percentage content of oxygen-containing inorganic components in SEI formed in PVM-GPE and PDE electrolytes. **d** 3D renders of LiO⁻, C₂HO⁻ in the TOF-SIMS sputtered volumes of the PVM-GPE induced SEI. **e** High-resolution TEM image of the forming SEI layer of the PVM-GPE, corresponding local fast Fourier transform image, and energy spectrum analysis. The SEI was characterized by assembling Li||Li symmetric cells and cycling them for 50 cycles at a current density of 0.5 mA cm⁻².

performance of the battery⁵³. Therefore, it is crucial to analyse the elemental composition and structure of the SEI layer formed by the electrolyte in order to understand the effect of the Li oxide dominated SEI layer content on the battery performance⁵⁴. X-ray Photoelectron Spectroscopy (XPS) is taken to profile the components of SEI formation from PVM-GPE and PDE electrolytes as shown in Fig. 3a, b and Supplementary Fig. 13. Major C-C (-284.8 eV), C-O (-286.5 eV), O=C-O (-288 eV), C=O (-290 eV) are detected in the C 1s XPS spectra in both electrolytes. However, the C 1s in PVM-GPE show RCO₃ (-291 eV) spectral peak, which mainly originates from the decomposition of the polymer. Li₂CO₃ signal is also detected in O 1s (-531 eV), indicating that the formed Li₂CO₃ is also an important component of SEI. It is noteworthy that the Li₂O intensity observed from the O 1s in PVM-GPE (-528 eV) is higher than that in the PDE electrolyte. The peak intensity decreases to some extent as the sputtering depth increases, suggesting that Li₂O is the primary component of the formed SEI. Specifically,

we also performed quantitative O-elemental analyses of the two electrolytes, PVM-GPE and PDE, and the results show that the percentage content of Li₂O is higher in PVM-GPE, with 76% and 28% before and after etching, respectively, which are both higher than that of PDE electrolyte (Fig. 3c). Meanwhile, the overall elemental quantitative analysis of the SEI of PVM-GPE (Supplementary Fig. 14) also show that the elemental O content increased from 66% to 74% with the increase of the etching depth. This further indicates that O is the main component in the SEI of PVM-GPE. As shown in the XPS spectrograms of B 1s and N 1s (Supplementary Fig. 15), the intensity of Li₃N (-398 eV) in PVM-GPE is higher than that observed in the PDE, revealing the participation of nitrification groups in PVM-GPE in the formation of SEI. In contrast, the peaks of B-O (191.5 eV), Li_xNO_y, and other N-O compounds mainly originated from the reductive decomposition of BOB⁻ and NO₃⁻. The homogeneity of the distribution of elements at the SEI interface in PVM-GPE can also be seen in Supplementary Fig. 16. The

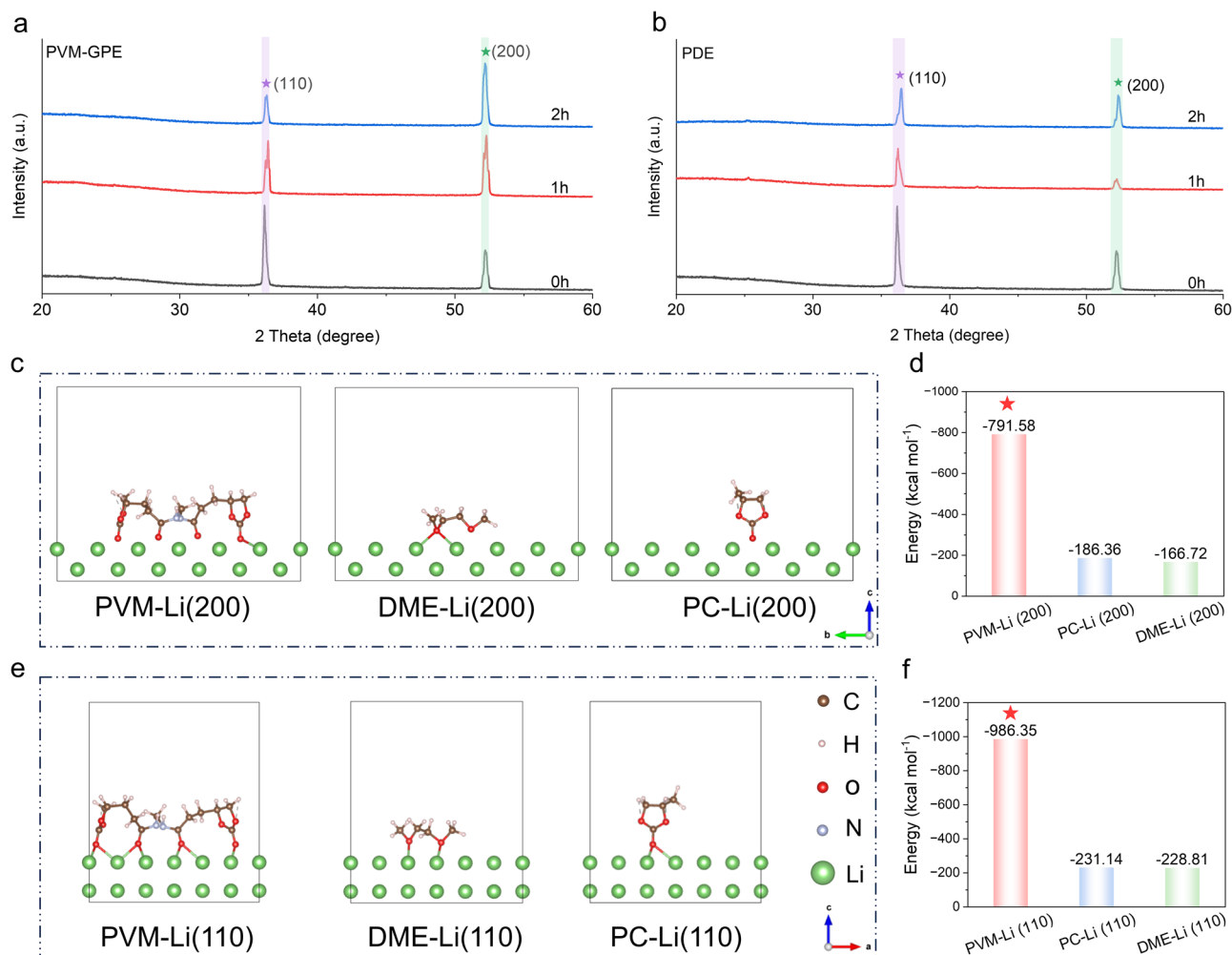


Fig. 4 | PVM-GPE with an F-free SEI layer induces preferential growth of the crystal planes of Li metals. Ex situ XRD patterns of crystal plane growth of Li metal ((110) and (200) deposited at 0 h, 1 h and 2 h using PVM-GPE (a) and PDE (b)

electrolytes. **c, d** Comparison of adsorption energies of PVM-GPE, DME and PC with Li (200) crystal planes. Comparison of adsorption energies of (e, f) PVM-GPE, DME and PC with Li (100) crystal planes.

compositional structure of SEI is further analyzed by depth profiling and 3D views using time-of-flight secondary ion mass spectrometry (TOF-SIMS) (Fig. 3d, and Supplementary Fig. 17). TOF-SIMS tests are consistent with the above results. SEI components with oxygen-containing O composition, can promote the uniform deposition of Li, inhibit side reactions between electrode interfaces, and serve to regulate the growth of Li metal along the planar ordered deposition⁵⁵.

Furthermore, Transmission Electron Microscopy (TEM) was employed to visualize the SEI structure and its local chemical composition of PVM-GPE (Fig. 3e). It was observed that PVM-GPE exhibited a uniform morphology of SEI, which facilitates uniform Li deposition at high areal capacities, ensuring stable cycling of Li metal batteries. Magnified images of the corresponding local surface crystal structure identified lattice fringes of Li₂O ((111) and Li₂O (200) with spacings of 0.267 nm and 0.231 nm, respectively. The lattice fringes of Li₂O not only confirm the presence of Li₂O in the SEI but also reveal the microstructural characteristics of the SEI. As an inorganic component, Li₂O is typically enriched in the inner layer of the SEI, in contact with the Li metal negative electrode. Li₂O helps guide ordered nucleation sites and reinforces the SEI. In particular, Selected Area Diffraction Electron (SADE) patterns from regions A and B of the PVM-GPE SEI further corroborated the presence of Li₂O. Elemental mapping via Energy-Dispersive Spectroscopy revealed significantly higher O content in the SEI derived from PVM-GPE. Collectively, they validate the microstructure of the SEI. Overall, the Li₂O inorganic and organic

components induced by PVM-GPE greatly promote uniform Li deposition and prevent parasitic reactions⁵⁶.

Characteristics of preferential direction growth at Li₂O-rich SEI interfaces

Fluorine-free SEI enriched with Li₂O are formed based on the unique solvated structural evolution of PVM-GPE. Subsequently, the crystal growth of Li₂O-dominated SEI on Li negative electrode is verified by X-ray Diffraction (XRD) tests. Ex situ XRD is employed to observe the evolution of the crystal planes in the Li || Li symmetric battery assembled with PVM-GPE and PDE electrolyte after 1 h and 2 h deposition (Fig. 4a and b). The primary crystal planes of Li metal are the (110) and (200) planes. Typically, the (110) plane exhibits lower energy, resulting in preferential growth of Li metal along this crystal plane. However, this inclination leads to unstable interfaces and uncontrollable Li dendrite growth⁵⁷. As expected, during the initial stages of Li deposition, the PDE electrolyte predominantly exhibits XRD peaks corresponding to the Li(110) crystal plane. As the deposition time of Li extends, the peak intensity of the (110) crystal plane tends to increase, indicating that the (110) crystal plane is the predominantly exposed plane. However, for the Li metal matched with PVM-GPE, the intensity of the (200) crystal plane gradually increases, while the intensity of the (110) plane decreases. This evidences that the (200) plane is the predominantly exposed crystal surface. During cycling, a preferential transition occurs from the (110) crystal plane to the (200) crystal

plane⁵⁸. The results of these surface energy calculations are shown in Figs. 4c–f and Supplementary Data 1. Surprisingly, PVM-GPE can modulate the energies of these crystallographic planes. Apparently, the energy relationship shifts to PVM-GPE(200) < PVM-GPE(110), indicating that the (200) plane now possesses the lowest surface energy. This finding suggests that PVM-GPE essentially reduces the surface energy, making the (200) plane the preferential orientation⁵⁹.

When PVM-GPE interacts with the Li(200) and Li(110) planes, its overall energy state is lower for the (200) plane compared to the (110) plane. This difference in energy states primarily stems from variations in atomic arrangement and bonding characteristics across the crystallographic planes. For the Li(200) plane, its atomic arrangement favors the formation of stable chemical bonds with components of Li₂O, thereby reducing the overall system energy⁶⁰. This results in a more stable SEI that effectively prevents co-intercalation of solvent molecules and protects electrode materials from damage. Due to the exposure of the plane with the lowest surface energy to the electrolyte, the reactivity of Li metal towards the electrolyte is suppressed, which assists shield adverse side reactions between Li metal and the electrolyte.

Depositional morphology and interfacial stability properties of asymmetric Li||Cu cells and symmetric Li||Li cells

Since the fluorine-free interface layer on PVM-GPE modulates the unique crystal plane growth mode, we test the interface performance by assembled Li||Li and Li||Cu cells to understand the stabilization mechanism. The uniform stability of Li stripping/plating for Li||Cu asymmetric cells is further explored under different current densities and surface capacities. At 0.5 mA cm⁻² current density and 0.5 mAh cm⁻² plating capacity, after 200 cycles, PVM-GPE show high average Coulombic efficiency (CE) (94.8%) (Fig. 5a). Notably, as the current density increases to 1 mA cm⁻², PVM-GPE provides a high average CE of 95.27% over 100 cycles (Supplementary Fig. 18). High Li-ion migration rate leads to more uniform Li deposition morphology, thereby enhancing the average Coulombic efficiency. This underscores the decent compatibility between PVM-GPE and Li⁺⁶¹. In contrast, the irreversible reaction between the PDE electrolyte and Li makes CE appear severe fluctuation. This adequately supports the reversibility of PVM-GPE with a stable long-term cycling. The critical current density of Li||Li symmetric cells is tested to attest to the ability of PVM-GPE to inhibit Li dendrites. It is observed from Fig. 5b that the PVM-GPE displays overpotential protection rather than short-circuiting at 3 mA cm⁻² with increasing current density, indicating that the better inhibition of disordered dendrite growth by the PVM-GPE interfacial layer component.

To further highlight the interfacial performance of PVM-GPE, we evaluated its rate performance in Li||Li symmetric batteries under various current densities (Fig. 5c). The finding reveals that, owing to the promotion of stable SEI formation and rapid Li⁺ conduction by PVM-GPE, it offers high durability by effectively protecting the Li metal interface from the electrolyte. The stability of the electrolyte to the Li metal negative electrode is verified at a fixed current of 1 mA cm⁻² and a plating capacity of 1 mAh cm⁻² (Fig. 5d). As anticipated, the cell assembled with PVM-GPE demonstrated stable Li plating/stripping for over 1500 h (750 cycles) at a polarization voltage of 0.26 V. Notably, the system also demonstrates stable Li plating/stripping for over 100 h even at an elevated current density of 3 mA cm⁻². This reveals that PVM-GPE has competitive compatibility with Li metal (Fig. 5e). Further, the interfacial impedance of Li||Li cells assembled based on PVM-GPE and PDE electrolytes at a fixed current density of 1 mA cm⁻² is measured by EIS after Li plating/stripping (impedance tested every 10 cycles). Notably, the Li|PVM-GPE|Li cell interfacial impedance gradually decreases, corresponding to a lower overpotential, which can be attributed to more stability of electrolyte against Li metal in the cell (Fig. 5f). Under the same conditions, the interfacial impedance of the

PDE electrolyte with Li metal increases and then decreases, illustrating the inhomogeneous deposition of Li⁺ (Supplementary Fig. 19). The interfacial Li⁺ transfer kinetics is not only related to the interfacial impedance of the electrolyte, but also to the electrode/electrolyte exchange current density⁶². As can be seen from the Tafel curve in Fig. 5g, the exchange current density of PVM-GPE (0.41 mA cm⁻²) is higher than that of PDE (0.12 mA cm⁻²). The results indicate that PVM-GPE has higher dielectric Li⁺ deposition and cyclic CE. The robust interfacial layer protects Li metal and regulates Li⁺ transport between electrolyte and electrode. The above experimental results show that the generation of Li₂O-dominated fluorine-free SEI layer by PVM-GPE can reduce the surface diffusion energy barrier of Li⁺ and accelerate the formation of interfacial Li⁺. These phenomena support the predominance of PVM-GPE in stabilizing the Li/electrolyte interface and enhancing the Li plating/stripping kinetics, contributing to the formation of uniform, smooth and dense Li deposition morphology⁶³.

SEM tests are performed to observe the morphology of Li metal deposition-exfoliation. Consistent with the above results, the PVM-GPE deposited on the Cu foil show a spherical structure with a dense and flat morphology (Fig. 5h). In sharp contrast, the Li deposition of the PDE electrolyte show irregular deposition with cracks, forming a loose deposition pattern. The major function of the PVM-GPE interfacial layer in regulating the reversible dense deposition of Li is abundantly revealed (Fig. 5i). The SEM image of the Li-Li cell at 1 mA cm⁻² shows that the Li metal surface of the PVM-GPE cycle is uniform and flat, and there is no obvious Li dendrite growth, which is consistent with the cross-sectional view of the SEM image. Scanning electron microscope (SEM) images of the Li symmetric battery after Li plating/stripping exhibit that the Li metal surface of the PVM-GPE is uniform and flat, with no obvious Li dendrite growth. The same can be observed from the cross-section of the test SEM images. This denser planar surface reduces the occurrence of side reactions and thus improves cycling stability. The Li electrode in contact with the PDE had a rough surface and an unstable interface. The above results indicate that the interfacial layer formed by PVM-GPE has the advantage of interfacial stability.

Cycling performance of full batteries under practical conditions of application

Given the solid SEI interface advantages of PVM-GPE, we further evaluate its practical applicability by assembling full cells. Figure 6a demonstrates the rate performance of the Li||NCM811 full cell assembled with PVM-GPE. The discharge capacities of this cell are 196.4, 192, 180.4, 168.6, 150, 136.7 and 117.1 mAh g⁻¹ at 0.1, 0.2, 0.5, 1, 2, 3 and 5 C, respectively (Supplementary Fig. 20). Upon the current was restored to 0.1C, the battery retained more than 99% of its capacity, indicating adequate stability and reversible performance. Furthermore, we evaluate the long-term cycling stability of the Li|PVM-GPE|NCM811 battery at a high rate of 3 C, as shown in Fig. 6b and Supplementary Fig. 21. The Li||NCM811 battery achieve a capacity retention rate of 84.7% after 800 cycles. This remarkable durability indicates that the Li₂O-rich SEI has a stable effect on Li metal, aligning with the results in Li||Li symmetric batteries. Furthermore, for maximum application practicability, PVM-GPE should be able to match high loaded positive electrode, high cut-off voltage and high nickel positive electrode. Therefore, we assemble the full cell with a high loaded NCM811 positive electrode at 8 mg cm⁻². the Li|PVM-GPE|NCM811 cell still achieves a specific capacity of 149.5 mAh g⁻¹ (Fig. 6c). Notably, competent cycling performance is achieved at a charge cut-off voltage of 4.5V at 0.5C current density. This ensures that the PVM-GPE can support the performance requirements of 4.5 V-grade high-voltage Li metal batteries (Fig. 6d, Supplementary Fig. 22). In order to test the operational requirements of PVM-GPE under higher nickel positive electrode conditions, the cell was assembled with NCM90 as the positive electrode to evaluate its cycling stability (Fig. 6e). This exhibits

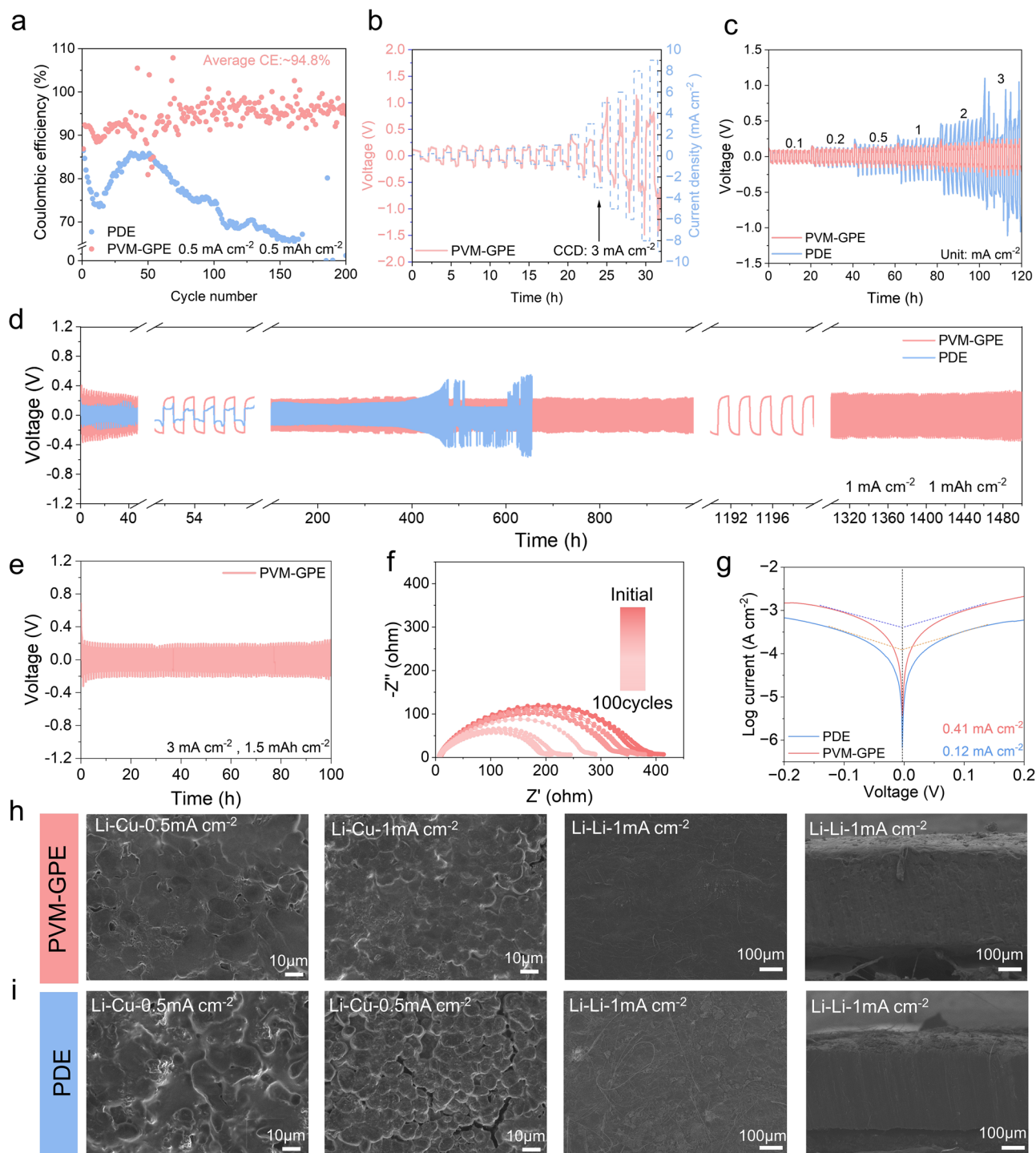


Fig. 5 | Interfacial electrochemical properties of fluorine-free SEI layers.

a Coulombic efficiency comparison of Li deposition/stripping for Li||Cu cells with PVM-GPE and PDE electrolyte at 0.5 mA cm^{-2} . **b** Critical current density (CCD) curves of Li||Li cells for PVM-GPE. **c** Rate performance of Li||Li symmetric batteries using PVM-GPE and PDE electrolytes. **d** Cycle voltage curves of Li||Li symmetric

cells with PVM-GPE and PDE electrolytes at 1 mA cm^{-2} . **e** Cycle voltage curve of Li||Li symmetric cell of PVM-GPE at 3 mA cm^{-2} . **f** Nyquist plots of PVM-GPE during Li plating/stripping cycling at 0.5 mA cm^{-2} for 1–100 cycles. **g** Tafel curves of PVM-GPE and PDE. SEM images of PVM-GPE (**h**) and PDE (**i**) after 100 h of cycling of Li||Cu and Li||Li cell at different current densities.

that PVM-GPE achieves the same acceptable cycling cycles at 0.5 C . Due to its robust fluorine-free interface, the PVM-GPE battery exhibits tolerable cycle stability even under harsh conditions. To further test the application potential of the PVM-GPE, we assemble and test pouch batteries. Notably, the Li|PVM-GPE|NCM811 pouch cell exhibits an impressive discharge capacity of up to 208 mAh g^{-1} at 0.2 C within the voltage range of $2.8\text{--}4.3 \text{ V}$, while the single-layer pouch cell can

achieve stable cycling for over 150 cycles (Fig. 6f, g). Additionally, the pouch battery of the PVM-GPE was subjected to abuse testing in order to evaluate the safety performance of the battery. As shown in Supplementary Fig. 23, the pouch battery illuminated the light-emitting diode even under bending, folding and cutting conditions. This reveals great utility. The assembled 1 Ah soft pack battery is shown in Fig. 6h and Supplementary Fig. 24. The pouch cell offers high cell capacity of

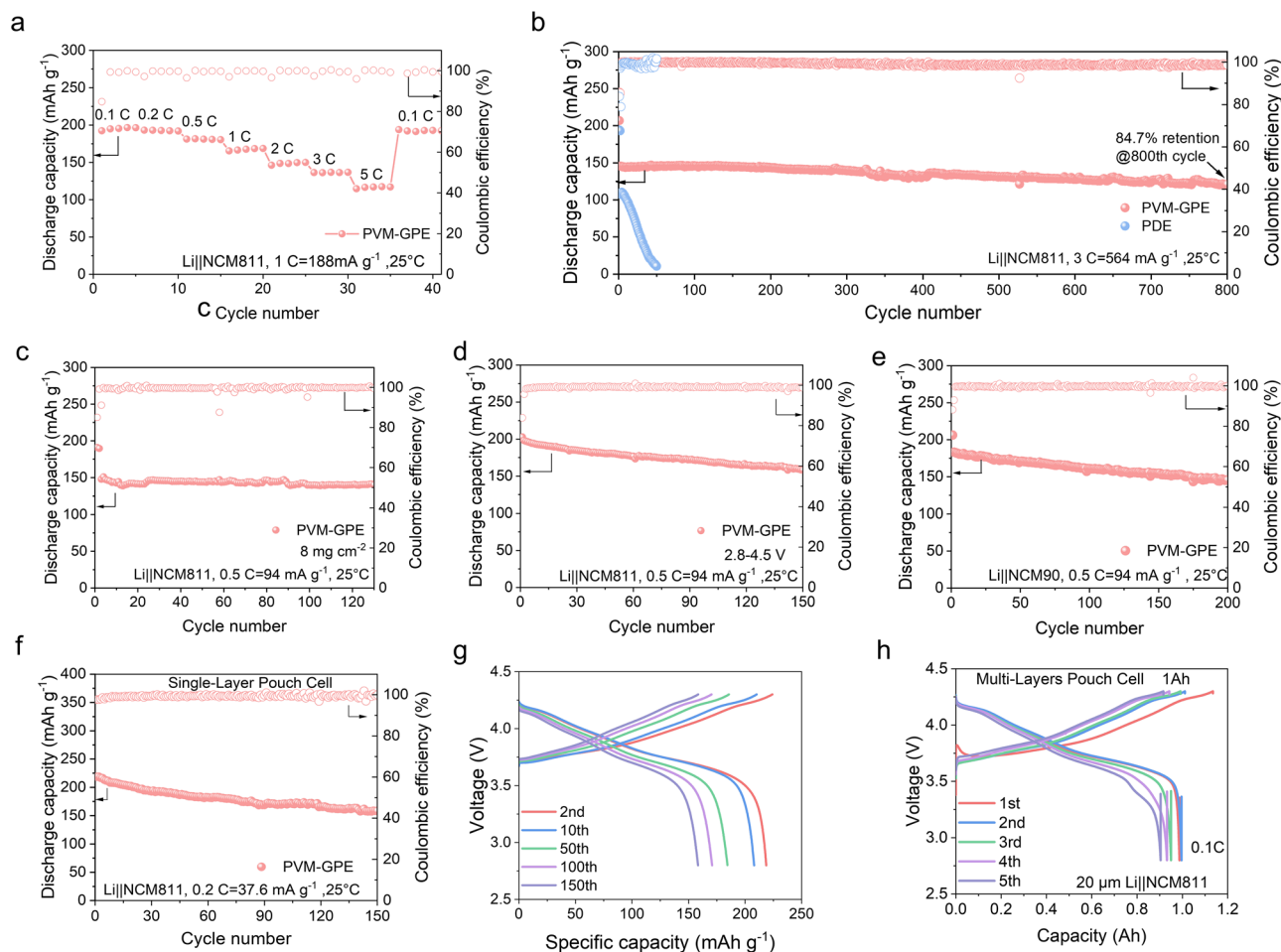


Fig. 6 | Application of F-free SEI based on PVM-GPE in Li metal batteries. **a** Rate Performance of Li|PVM-GPE|NCM811 cell. **b** Cycling performance of Li|NCM811 cells with PVM-GPE and PDE electrolytes at 3 C. The cutoff voltage is 4.3 V. **c** Cycling performance of 4.3 V Li|PVM-GPE|NCM811 cells at 0.5 C using positive electrode with high mass loadings. **d** Cycling performance of 4.5 V Li|PVM-GPE|NCM811 cells at 0.5 C. **e** Cycling performance of 4.3 V Li|PVM-GPE|NCM90 cells at 0.5 C. **f** Cycling

performance of the Li|PVM-GPE|NCM811 pouch battery at 0.2 C. **g** Charge-discharge profiles of Li|PVM-GPE|NCM811 pouch cells at different cycles. **h** Cycling performance of the Li|PVM-GPE|NCM811 1 Ah pouch battery. (Unless specifically noted otherwise, the areal loading of the battery positive electrode is approximately 3 mg cm^{-2} , $1 \text{ C} = 188 \text{ mA g}^{-1}$ (NCM811), $1 \text{ C} = 200 \text{ mA g}^{-1}$ (NCM90)).

up to 0.996 Ah. These demonstrate the great potential of the PVM-GPE for practical applications. The rugged SEI achieves respectable performance for sustainable battery applications.

Interfacial stability behaviour analysis of high nickel positive electrodes

A dense and robust CEI reduces side reactions between transition metal elements such as high nickel and the electrolyte interface⁶⁴. To investigate the mechanism of action by which PVM-GPE matches the high-nickel positive electrode at high voltage, we used TEM to monitor the formation of CEI on the positive electrode (Supplementary Fig. 25). As shown in Fig. 7a, a uniform CEI with a thickness of ~7 nm was formed on the positive electrode surface employing PVM-GPE electrolyte. This structurally compact interfacial layer effectively suppresses electrolyte oxidative decomposition under high-voltage conditions, thereby significantly enhancing its compatibility with high-nickel positive electrode materials. Comparative analysis reveals that the CEI layer formed on NCM811 positive electrode with PDE electrolyte exhibits distinct inhomogeneity (Fig. 7b), which shows direct correlation with their cycling performance degradation in high-nickel systems. Further SADE analysis demonstrates that NCM811 positive electrode in PDE electrolyte systems undergo noticeable structural degradation during cycling, while the PVM-GPE-based electrolyte system effectively maintains long-term structural stability of the NCM811 positive

electrode material (Supplementary Fig. 26). To analyze the composition of the CEI, XPS testing was conducted on the NCM811 positive electrode after cycling with PVM-GPE. In the C 1 s, O 1 s, F 1 s, N 1 s, and B 1 s spectra (Fig. 7c, d and Supplementary Fig. 27), inorganic components such as Li_3N , C-O, C=O, N-O, appeared on the positive electrode surface after PVM-GPE cycling. These components primarily originate from the decomposition of PVM-GPE. The presence of B-O in the B 1 s spectrum indicates that more BOB anions are involved in the formation of the CEI. It is noteworthy that as the Ar^+ etching time increases, the C-F component in the F 1 s spectrum further increases. However, the LiF component remains almost unchanged, which is attributed to the PVDF binder formed on the positive electrode surface. Eventually, elemental analysis was also conducted on the overall CEI composition (Supplementary Fig. 28). Interestingly, the F content is ~5%. This indicates that the primary elements of the CEI formed by PVM-GPE are C and O. Due to these elements forming a uniform and robust CEI, it effectively inhibits the structural collapse caused by volume expansion of the NCM811 particles, enabling the Li|NCM811 battery assembled with PVM-GPE to cycle stably at high rates.

Subsequently, the lattice changes of NCM811 are revealed by in situ XRD (Fig. 7e). (003) is the main characteristic diffraction peak of NCM811 with an offset of 0.43° . The small offset indicates that the anisotropic volume change is small. Therefore, NCM811 containing PVM-GPE has less volume change during the cycling process, which

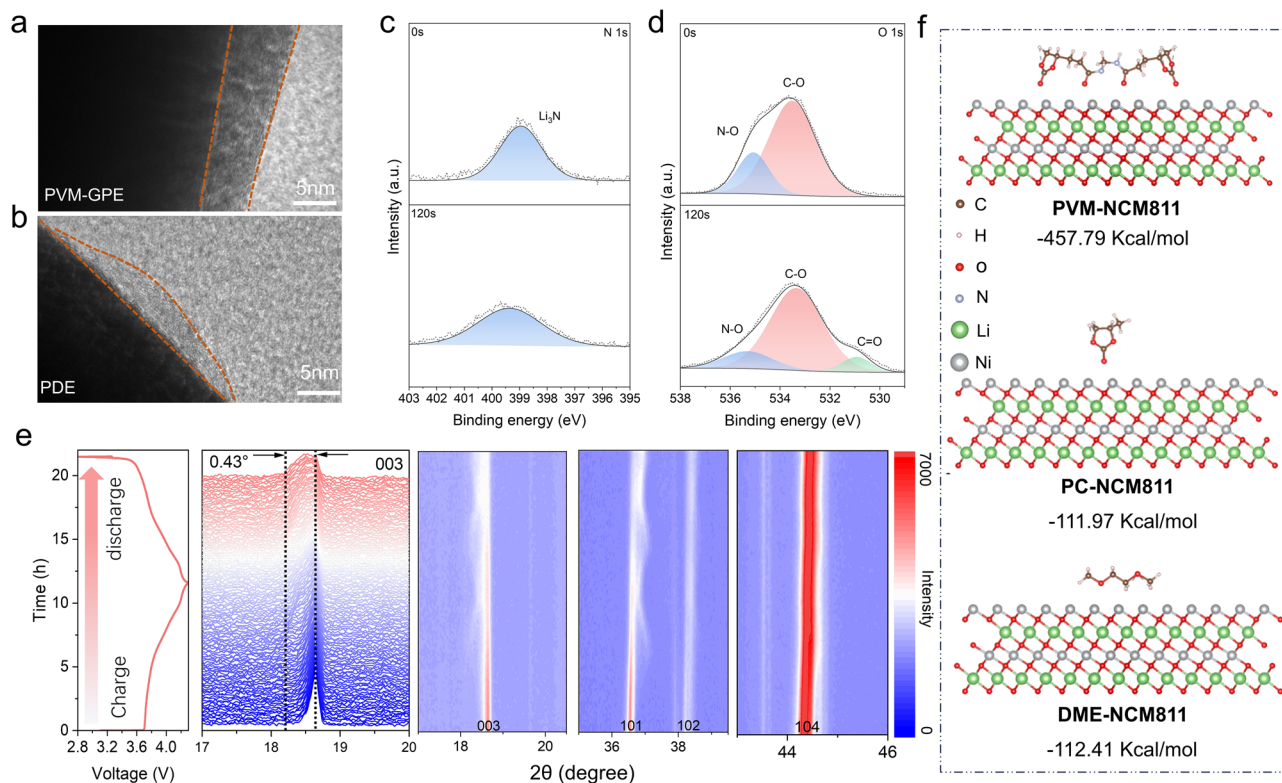


Fig. 7 | Mechanism of stabilization of high Ni positive electrode by PVM-GPE. **a, b** TEM image of NCM811 positive electrode of PVM-GPE (**a**) and PDE electrolyte (**b**) after 50 charge and discharge cycles at 0.1 C, 4.3 V; (**c, d**) XPS spectra of N 1s (**c**) and O 1s (**d**) of NCM811 positive electrode using PVM-GPE discharge followed by 50

cycles 0.1 C, 4.3 V; (**e**) In situ XRD pattern of NCM811 positive electrode assembled by PVM-GPE at 0.2 C. **f** Scheme of adsorption status for different components on NCM811 surface.

effectively inhibits the structural collapse due to the volume expansion of NCM811 particles⁶⁵. In addition, the evolutionary trends of the characteristic diffraction peaks of (003), (101), (102), and (104) are consistent with the long-cycle stability of their cells. Furthermore, the adsorption energies of the electrolytes of different compositions with NCM811 crystal faces are also calculated by further DFT (Fig. 7f and Supplementary Data 1). It is evident that the adsorption energy of PVM-GPE on the NCM811 (003) crystal surface is the maximum. Thus, PVM-GPE is more likely to adsorb and react on NCM811 during the cycling process to produce CEIs rich in C, B and O components⁶⁶.

In summary, we present a polymer electrolyte based on molecular design principles to construct highly stable cycling Li-metal batteries by a fluorine-free SEI. Cross-linked copolymers consisting of highly polar cyclic VC and MBA are utilised to boost the coordination of Li⁺. Simultaneously, the crosslinker reinforces the anion adsorption effect through hydrogen bonding interactions as to achieve higher Li⁺ transfer (0.77) for PVM-GPE. This fluorine-free SEI delivers fast Li⁺ transport kinetics and reduces the occurrence of undesirable interfacial reactions. Moreover, the Li metal negative electrode preferentially grows from the (200) plane as monitored by XRD, which promotes uniform deposition of Li⁺ and enables highly reversible Li plating/stripping. Quantitative XPS analysis of the percentage of elemental oxygen content in SEI confirms that the high Li₂O content in SEI corresponds to the long cycle stability of the battery. Based on this property, the Li|PVM-GPE|Li symmetric cell attained a long cycle stability of 1500 h at 1 mA cm⁻². Assembled Li|PVM-GPE|NCM811 cell cycling 800 times reaches 84.8% retention rate at 3 C. The cycling stability of the recently as-developed PVM-GPE at high rate compares to that of mainstream fluorine-based polymer electrolytes. Particularly, the respectable cycling performance of the pouch cell reflects its

potential for practical applications. Therefore, the PVM-GPE we proposed, by constructing a fluorine-free SEI, significantly enhances the stability of the negative electrode interface, thereby laying a solid foundation for the design of quasi-solid-state batteries that are sustainable for development.

Methods

Materials

N, N'-Methylenebisacrylamide (MBA, 98%), Azodiisobutyronitrile (AIBN, 98%) are purchased from Shanghai Macklin Biochemical Co., Ltd. Vinylene carbonate (VC, 99.99%), Propylene carbonate (PC, 99.99%), 1,2-Dimethoxyethane (DME, 99.99%), Linitrateare (LiNO₃, 99.99%), positive electrode(NCM811/NCM90, 99.9%), conductive agent(Super P Li, 99.9%), and binder(PVDF, Mw = 1.5 million, 99.9%) lithium metal foil with a thickness of 0.45 mm and 1Ah Li|NCM811 pouch battery are purchased from Guangdong Canrd New Energy Technology Co. Ltd. Li bis(oxalate)borate (LiBOB, 99%) is purchased from Shanghai Aladdin Biochemical Technology Co., Ltd. Glass fiber separator (Whatman, GF/C, thickness = 260 μm). All reagents were used as received without further purification.

Preparation and synthesis of electrolytes

PDE electrolyte. The PDE electrolyte was prepared with 1.0 mol/L LiBOB + 0.2 mol/L LiNO₃ in PC/DME mixed solvent (1:3 by volume). All electrolytes were fabricated in an argon-filled glovebox (O₂ < 0.1 ppm, H₂O < 0.1 ppm) at ambient temperature.

Synthesis of PVM gel polymer electrolyte (PVM-GPE). The VC monomer was added into a small glass vial, followed by the addition and mixing of MBA monomer at a 2% molar ratio to VC. Subsequently, an equal volume of PDE electrolyte was incorporated to form the

precursor solution. Then, 0.5% by weight of azobisisobutyronitrile (AIBN) was dissolved in this mixture. The resulting solution was maintained at 70 °C under an argon atmosphere for 6 h to obtain poly(vinylene carbonate-co-N,N'-methylenebisacrylamide) (PVM). The prepared precursor solution was dispensed in an amount of 70 microliters onto a glass fiber separator (Whatman), and subsequently, the battery was assembled under the same temperature and time conditions as mentioned above. After gelation, the battery was allowed to stand for 12 h before testing to ensure uniform distribution of the electrolyte within the battery. Polymer electrolyte membranes were fabricated to match the thickness of glass fiber separators (260 μm).

Positive electrode prepared. The positive electrode slurry was prepared by mixing the positive electrode material powder (NCM811/NCM90, 800 mg), Super P (100 mg), and PVDF (100 mg) at an 8:1:1 mass ratio in 2.5 mL of NMP solvent using a hybrid defoaming mixer (AR-100). The slurry was then cast onto aluminum foil using a 200 μm doctor blade to fabricate the positive electrode, which was dried in a vacuum oven at 80 °C for 12 h. The resulting positive electrode had a mass loading of 3 mg cm^{-2} . For the NCM811 positive electrode with a higher mass loading of 8 mg cm^{-2} , the same ratio and procedure were followed, but a 500 μm doctor blade was used for coating. The prepared electrodes were cut into 12 mm discs using a manual cutting machine (Shenzhen Kejing, MSK-T10). The mixing, casting, and cutting processes were all conducted under ambient atmosphere and room temperature.

Battery assembly

The coin cell employs a stainless-steel casing of the CR2032 type. Its electrodes consist of a single-side-coated positive electrode ($\Phi 12$ mm) paired with a lithium foil negative electrode ($\Phi 15.6$ mm), separated by a glass fiber separator (Whatman, GF/C, 260 μm). After injecting 70 μL of precursor solution, the cell is assembled under a sealing pressure of 60 kg cm^{-2} , followed by a 6-hour static rest at 70 °C. The single-layer pouch cell is assembled using a sandwich stacking process (positive electrode/separator/negative electrode), with 800 μL of electrolyte injected. It is then vacuum-sealed under conditions of 160 °C/3 MPa. During cyclic testing, an external pressure of 1.0 MPa is applied using a rigid fixture. The testing process for the multi-layer pouch cell is consistent with that of the single-layer pouch cell. The 1 Ah pouch cells used in this study were purchased from Guangdong Kaide New Energy Technology Co., Ltd. (supplier). They are electrolyte-free dry-state cells with specifications of NCM811 + lithium metal system, manufactured using the lamination process, and model number 425868. Before the introduction of PVM-GPE, no liquid or solid electrolytes were pre-existing in the cells. These batteries were assembled in a “dry state” (containing only electrodes, separators, and aluminum-plastic film casings, without any electrolytes) to eliminate interference from other electrolyte components. This dry cell consists of 15 layers of electrodes (7 layers of double-sided coated positive electrode material, with an areal density of 17.7 mg cm^{-2} ; 8 layers of lithium metal negative electrode, with a thickness of 20 μm and a theoretical single-sided areal capacity of 4.1 mAh cm^{-2}), with an N/P ratio of ~3.6. The separator used is a PP separator. PVM-GPE was injected into the dry-state pouch cells through the following steps: In a glove box environment, about 3 mL of the precursor solution was injected through the reserved liquid injection port, followed by standing for 1 hour to ensure that the precursor solution fully wets the electrode pores and the separator, achieving close contact with the electrodes. After the wetting was completed, the cells were heated at 70 °C for 6 h to initiate the cross-linking reaction of the polymer matrix, converting the precursor into a quasi-solid state. Finally, the liquid injection port was sealed using a heat-sealing process to complete the battery assembly. A pressure of ~250 kPa was applied during the cycling of the pouch cells. The entire

battery assembly process was completed in an argon atmosphere glove box ($\text{O}_2 < 0.1$ ppm, $\text{H}_2\text{O} < 0.1$ ppm).

Materials characterization

The structure of the electrolyte was investigated by FTIR spectroscopy using Bruker, Germany. Differential scanning calorimetry (METTLER, Switzerland) and thermogravimetry (METTLER, Switzerland) were used to monitor the thermal stability of the solid electrolytes under nitrogen flow with a heating rate of 10 °C/min. DSC test was conducted under a nitrogen atmosphere. The temperature range was set from -70 °C to 100 °C, and the heating rate was increased to enhance resolution. A heating rate of 20 K/min was employed, which aids in characterizing the material's glass transition temperature with higher resolution. The polymer material was subjected to TGA testing by heating it from 25 °C to 800 °C at a rate of 10 K/min in a nitrogen atmosphere. The surface morphologies of cycled Li metal negative electrode, positive electrode sheets, and electrolytes were analyzed using a JSM-7800F field-emission scanning electron microscope (SEM-EDX, JEOL, Japan). The measurements were performed at an accelerating voltage of 5 kV to optimize spatial resolution and minimize beam-induced damage. Cycled positive electrode materials were dissolved in acetone and uniformly dispersed via ultrasonication. A droplet of the dispersed solution was deposited onto a Cu grid, followed by natural evaporation of acetone prior to TEM observation using a JEM-F200 TEM (JEOL, Japan). Samples for X-ray Photoelectron Spectroscopy (XPS) analysis were prepared under inert atmosphere to minimize surface oxidation, mounted on conductive tape, and transferred via an air-tight transfer vessel to ensure ambient-free conditions. The measurements were performed using a Thermo Fisher Scientific K-Alpha+ spectrometer equipped with a monochromatic Al K α source, operated at 15 kV and 10 mA emission current. Charge compensation was achieved using a dual-beam electron/Ar+ flood gun, and energy calibration was referenced to the C 1s peak at 284.8 eV. In situ X-ray Diffraction (XRD): Performed on a PANalytical Empyrean diffractometer (Malvern Panalytical, Netherlands) with Cu K α radiation ($\lambda = 1.5406$ Å). The assembled cell was fixed on an in situ stage, ensuring parallel alignment between the X-ray window and electrode surface. Scans were conducted at 10°–80° (2 θ) with a scan rate of -0.25°/s during galvanostatic cycling at 0.2 C, with intermittent XRD pattern collection. We assembled Li|NCM811 coin cells with a 12 mm diameter cathode window and performed the initial cycle test at 25 °C and 0.2 C rate, while monitoring the crystallographic evolution of cathode materials through in situ XRD characterization. Ex situ XRD: we assembled Li|Li symmetric cells and disassembled them after 0, 1, and 2 h of plating/stripping at a current density of 1 mA cm^{-2} under 25 °C to perform XRD measurements. Surface chemistry of cycled Li metal negative electrode and positive electrode was analyzed using a Thermo Scientific K-Alpha+ spectrometer (UK) with Al K α excitation (1486.6 eV). A PHI nanoTOF II Time-of-Flight Secondary Ion Mass Spectrometer (TOF-SIMS) manufactured by ULVAC in Japan to conduct a detailed analysis of the surfaces of the cycled Li metal negative electrode and positive electrode materials. A Bi⁺ ion beam was first accelerated with an energy setting of 30 keV to achieve high-sensitivity excitation of the sample surface. Subsequently, a Cs⁺ ion beam was used to sputter the sample under sputtering conditions of 3 keV voltage and 100 nA current.

Electrochemical characterization

The electrochemical impedance spectroscopy (EIS) measurements were conducted with an AC perturbation signal of 10 mV amplitude under potentiostatic mode, with a frequency range from 100 kHz to 0.1 Hz. The data were acquired at a density of 10 points per decade (logarithmic distribution), totaling 70 data points. Prior to measurement, the samples were stabilized at open circuit potential for 1 hour to ensure steady-state conditions. The testing temperatures were ranged

from 25 to 100°C and the ionic conductivity σ is calculated by the following equation:

$$\sigma = \frac{L}{SR} \quad (1)$$

where L represents the thickness (cm) of the electrolyte membrane, R represents the bulk resistance (Ω), and S corresponds to the contact area (cm^2) between SS and electrolyte. The impedance spectra were measured by scanning in a frequency range from 0.1 Hz to 100 kHz in the symmetrical Li||Li cells. The linear sweep voltammetry (LSV) measurements were conducted at a sweep rate of 1 mV s^{-1} from 2 to 6 V. The leakage current test was conducted in Li||NCM811 cells with different electrolytes. The cells were charged to various voltages and then held at each voltage for 36,000 s while monitoring the current using a CH Instruments (Shanghai) electrochemical workstation. The Tafel plots of Li||Li symmetric cells in different electrolyte systems were measured at a scan rate of 1 mV s^{-1} . The Li||NCM811/90 cells were assembled with lithium metal as the anode and NCM811/90 sheets as the cathode. The cells were initially cycled twice at 0.1 C, followed by cycling at different rate within voltage ranges of 2.8–4.3 V and 2.8–4.5 V. For Li||Cu cells, Cu foils with a diameter of 14 mm were employed. The Coulombic efficiency (CE) test was performed using Li||Cu cells, where lithium ions were first deposited onto the Cu foil via constant-current discharge at varying current densities, followed by stripping up to 1 V. Li||Li symmetric cells were assembled and applied a small polarization potential (ΔV) of 10 mV. During the experiment, the initial polarization current (I^0) and steady-state polarization current (I^{ss}) were recorded respectively. Through EIS analysis before and after potentiostatic polarization testing, we systematically characterized the variations in bulk resistance (R_0^b before polarization and R_{ss}^b after polarization) and electrode/electrolyte interfacial resistance (R_0^i before polarization and R_{ss}^i after polarization). Based on these experimental data, the lithium ion transference number (t_{Li^+}) was calculated using the following equation:

$$t_{Li^+} = \frac{I^{ss}(\Delta V - I^0 R_i^0)}{I^0(\Delta V - I^{ss} R_i^{ss})} \quad (2)$$

Theoretical calculation

The geometric structures of all molecules were fully optimized using the hybrid B3LYP functional with the 6-31 G(d, p) basis set in GaussView 5.0 software. Density functional theory (DFT) was employed for the visual calculation of electrostatic potential maps, LUMO-HOMO energy levels, and binding energies. To simplify the computational model, a repeating unit from a polymer chain was selected as the calculation model for the polymer matrix. The convergence criteria were as follows: the SCF convergence threshold was set to $\Delta E < 1 \times 10^{-9}$, and the change in the density matrix was ensured to be less than 1×10^{-5} . Additionally, geometric optimization was carried out using Opt+Freq to ensure force convergence ($\text{RMS} < 1 \times 10^{-4}$) and displacement convergence ($\text{RMS} < 4 \times 10^{-4}$ Bohr). Frequency analysis was performed to exclude imaginary frequencies, ensuring strict convergence at the energy, electron density, and structural levels with an error margin of less than 0.01 eV.

In Materials Studio 2020, molecular dynamics simulations of the solvation structure of Li^+ in the electrolyte system were conducted using the Forcite module and the COMPASS II force field. Van der Waals interactions were treated using an atom-based method, while electrostatic interactions were calculated using the Ewald summation method with a cutoff radius of 12.5 Å. The equations of motion were integrated using a time step of 1 fs. The system was first subjected to energy minimization optimization, followed by a 400 ps equilibrium

simulation under the NPT ensemble ($P = 1 \text{ atm}$, $T = 333.15 \text{ K}$) with periodic boundary conditions. The Nose-Hoover thermostat and Berendsen barostat were employed to ensure sufficient relaxation of the system until temperature, potential energy, and total energy reached equilibrium. After equilibrium, the simulation was continued for another 400 ps under the NVT ensemble for data collection. Trajectory files were output at 4 ps intervals and used for statistical analysis of radial distribution functions (RDFs) and coordination numbers (CNs). For adsorption energy calculations using the DMol3 module in Materials Studio 2020, a surface adsorption model was first constructed: the substrate material was cleaved along the (200) and (110) planes of Li, creating a surface with two atomic layers measuring $15 \times 10 \times 17 \text{ \AA}$. A vacuum layer of 15 Å was added perpendicular to the surface to eliminate interactions arising from periodic boundary conditions. The computational parameters were set as follows: the exchange-correlation energy was treated using the Perdew-Burke-Ernzerhof (PBE) functional within the generalized gradient approximation (GGA) framework, and electron interactions were handled using an all-electron relativistic core treatment. The double numerical plus polarization (DNP) basis set was selected to ensure computational accuracy. The self-consistent field (SCF) calculation convergence criterion was set to $1.0 \times 10^{-6} \text{ Ha}$, and geometric optimization was performed using the conjugate gradient method with convergence thresholds of $1.0 \times 10^{-5} \text{ Ha}$ for energy, 0.002 Ha/\AA for force, and 0.005 \AA for displacement. To accurately describe adsorption behavior, van der Waals corrections (such as the TS or D3 method) were considered, and Fermi level broadening (0.005 Ha) was applied to improve convergence. The adsorption energy was calculated using the formula $E_{\text{ads}} = E_{\text{total}} - (E_{\text{slab}} + E_{\text{mol}})$, where all energy terms were optimized under the same computational parameters.

Data availability

Source Data file has been deposited in Figshare under accession code (<https://doi.org/10.6084/m9.figshare.29135531>) link.

References

- Zhou, Q. J. et al. Tailoring electric double layer by cation specific adsorption for high-voltage quasi-solid-state Li metal batteries. *Angew. Chem. Int. Ed.* **63**, e202402625 (2024).
- Liu, Y. et al. In situ polymerization of 1,3-dioxane as a highly compatible polymer electrolyte to enable the stable operation of 4.5 V Li-metal batteries. *Energy Environ. Sci.* **16**, 6110–6119 (2023).
- Li, J. L. et al. Understanding and regulating the mechanical stability of solid electrolyte interphase in batteries. *Adv. Energy Mater.* **15**, 2403845 (2024).
- Tu, S. et al. Fast-charging capability of graphite-based Li-ion batteries enabled by Li_3P -based crystalline solid-electrolyte interphase. *Nat. Energy* **8**, 1365–1374 (2023).
- Ko, S. et al. Electrode potential influences the reversibility of Li-metal anodes. *Nat. Energy* **7**, 1217–1224 (2022).
- Wan, H., Wang, Z., Zhang, W., He, X. & Wang, C. Interface design for all-solid-state Li batteries. *Nature* **623**, 739–744 (2023).
- Zhao, Q., Stalin, S. & Archer, L. A. Stabilizing metal battery anodes through the design of solid electrolyte interphases. *Joule* **5**, 1119–1142 (2021).
- Chen, L. et al. In situ construction of Li_3N -enriched interface enabling ultra-stable solid-state $\text{LiNi}_{0.8}\text{Co}_{0.1}\text{Mn}_{0.1}\text{O}_2/\text{Li}$ metal batteries. *Nano Energy* **100**, 107470 (2022).
- Hobold, G. M., Wang, C., Steinberg, K., Li, Y. & Gallant, B. M. High Li oxide prevalence in the Li solid-electrolyte interphase for high Coulombic efficiency. *Nat. Energy* **9**, 580–591 (2024).
- Xu, H. T. et al. The Role of the molecular encapsulation effect in stabilizing hydrogen-bond-rich gel-State Li metal batteries. *Angew. Chem. Int. Ed.* **63**, e202400032 (2024).

11. Zeng, H. et al. Beyond LiF: tailoring Li₂O-dominated solid electrolyte interphase for stable Li metal batteries. *ACS Nano* **18**, 1969–1981 (2024).
12. Wang, Z. et al. Li anode interlayer design for all-solid-state Li-metal batteries. *Nat. Energy* **9**, 251–262 (2024).
13. Li, Y. et al. Correlating structure and function of battery interphases at atomic resolution using cryoelectron microscopy. *Joule* **2**, 2167–2177 (2018).
14. Fan, X. et al. All-temperature batteries enabled by fluorinated electrolytes with non-polar solvents. *Nat. Energy* **4**, 882–890 (2019).
15. Wang, Y. et al. Fluorination in advanced battery design. *Nat. Rev. Mater.* **9**, 119–133 (2024).
16. Ajanovic, A. & Haas, R. Economic and environmental prospects for battery electric- and fuel cell vehicles: a review. *Fuel Cells* **19**, 515–529 (2019).
17. Bai, Y. et al. Energy and environmental aspects in recycling Li-ion batteries: concept of battery identity global passport. *Mater. Today* **41**, 304–315 (2020).
18. Wang, Y. et al. Fluorine chemistry in rechargeable batteries: challenges, progress, and perspectives. *Chem. Rev.* **124**, 3494–3589 (2024).
19. Qiao, R. et al. Non-fluorinated electrolytes with micelle-like solvation for ultra-high-energy-density Li metal batteries. *Chem* **11**, 102306 (2025).
20. Li, A.-M. et al. Methylation enables the use of fluorine-free ether electrolytes in high-voltage Li metal batteries. *Nat. Chem.* **16**, 922–929 (2024).
21. Yang, Y. et al. Dilute electrolytes with fluorine-free ether solvents for 4.5 V Li metal batteries. *Angew. Chem. Int. Ed.* **63**, e202409193 (2024).
22. Kufian, M. Z. et al. PMMA–LiBOB gel electrolyte for application in Li ion batteries. *Solid State Ion.* **208**, 36–42 (2012).
23. Arof, A. K. et al. Electrical double layer capacitor using poly(methyl methacrylate)–C₄BO₃Li gel polymer electrolyte and carbonaceous material from shells of mata kucing (*Dimocarpus longan*) fruit. *Electrochim. Acta* **74**, 39–45 (2012).
24. Gunathilaka, A. M. I. E., Bandara, L. R. A. K., Arof, A. K., Careem, M. A. & Seneviratne, V. A. Electrical and structural studies of a LiBOB-based gel polymer electrolyte. *Ionics* **23**, 2669–2675 (2017).
25. Borah, S., Guha, A. K., Saikia, L. & Deka, M. Nanofiber induced enhancement of electrical and electrochemical properties in polymer gel electrolytes for application in energy storage devices. *J. Alloy. Compd.* **886**, 161173 (2021).
26. Zhu, J. et al. Single-Ion conducting polymer electrolytes for solid-state Li–metal batteries: design, performance, and challenges. *Adv. Energy Mater.* **11**, 2003836 (2021).
27. Wan, H., Xu, J. & Wang, C. Designing electrolytes and interphases for high-energy Li batteries. *Nat. Rev. Chem.* **8**, 30–44 (2024).
28. Han, J. et al. Fluorine-containing phase-separated polymer electrolytes enabling high-energy solid-state Li metal batteries. *Adv. Funct. Mater.* **34**, 2310801 (2024).
29. Sun, H. et al. High-safety and high-energy-density Li metal batteries in a novel ionic-liquid electrolyte. *Adv. Mater.* **32**, 2001741 (2020).
30. Chen, X. et al. In situ polymerized fluorine-free ether gel polymer electrolyte with stable interface for high-voltage Li metal batteries. *Adv. Funct. Mater.* 2421965 <https://doi.org/10.1002/adfm.202421965> (2024).
31. Xu, H. et al. Mg²⁺ Initiated in-situ polymerization of dioxolane enabling stable interfaces in solid-state Li metal batteries. *Energy Environ. Sci.* **18**, 4231–4240 (2025).
32. Yang, S.-J. et al. Intrinsically safe Li metal batteries enabled by thermo-electrochemical compatible in situ polymerized solid-state electrolytes. *Adv. Mater.* **36**, 2405086 (2024).
33. Song, X. et al. Practical 4.7 V solid-state 18650 cylindrical Li metal batteries with in-situ fabricated localized high-concentration polymer electrolytes. *Natl. Sci. Rev.* **12**, nwaf016 (2025).
34. Meng, Y. et al. Designing phosphazene-derivative electrolyte matrices to enable high-voltage Li metal batteries for extreme working conditions. *Nat. Energy* **8**, 1023–1033 (2023).
35. Xu, H. et al. Deciphering and integrating functionalized side chains for high ion-conductive elastic ternary copolymer solid-state electrolytes for safe Li metal batteries. *Angew. Chem. Int. Ed.* **63**, e202406637 (2024).
36. Li, P. et al. Efficiencies of various in situ polymerizations of liquid electrolytes and the practical implications for quasi solid-state batteries. *Angew. Chem. Int. Ed.* **62**, e202309613 (2023).
37. Miao, X. et al. In situ gel polymer electrolyte with rapid Li⁺ transport channels and anchored anion sites for high-current-density Li-ion batteries. *Adv. Funct. Mater.* **35**, 2411751 (2025).
38. Peng, H. et al. Molecular design for in-situ polymerized solid polymer electrolytes enabling stable cycling of Li metal batteries. *Adv. Energy Mater.* **14**, 2400428 (2024).
39. He, Y. et al. In-situ formation of quasi-solid polymer electrolyte for wide-temperature applicable Li-metal batteries. *Energy Storage Mater.* **68**, 103281 (2024).
40. Yu, Z. et al. Molecular design for electrolyte solvents enabling energy-dense and long-cycling Li metal batteries. *Nat. Energy* **5**, 526–533 (2020).
41. Choi, I. R. et al. Asymmetric ether solvents for high-rate Li metal batteries. *Nat. Energy* <https://doi.org/10.1038/s41560-025-01716-w> (2025).
42. Du, M., He, Z., Zhang, Y., Cai, Y.-P. & Zheng, Q. Sustainable release of LiNO₃ from a fluorine-decorated metal–organic framework separator to enable high-performance Li-metal batteries in carbonate electrolytes. *Adv. Energy Mater.* **15**, 2403674 (2025).
43. Li, J. et al. Prospective application, mechanism, and deficiency of Li bis(oxalate)Borate as the electrolyte additive for Li-batteries. *Adv. Energy Mater.* **13**, 2301422 (2023).
44. Xie, K. et al. Controlling the supramolecular architecture enables high Li cationic conductivity and high electrochemical stability for solid polymer electrolytes. *Adv. Funct. Mater.* **34**, 2315495 (2024).
45. Zhang, W. et al. In-situ polymerized gel polymer electrolytes with high room-temperature ionic conductivity and regulated Na⁺ solvation structure for sodium metal batteries. *Adv. Funct. Mater.* **32**, 2201205 (2022).
46. Chen, L. et al. Homogeneous polymer-ionic solvate electrolyte with weak dipole-dipole interaction enabling long cycling pouch Li metal battery. *Nat. Commun.* **16**, 3517 (2025).
47. Chen, Y. et al. Cosolvent occupied solvation tuned anti-oxidation therapy toward highly safe 4.7 V-class NCM811 batteries. *Energy Environ. Sci.* **17**, 6113–6126 (2024).
48. Chen, Y. et al. Breaking solvation dominance of ethylene carbonate via molecular charge engineering enables lower temperature battery. *Nat. Commun.* **14**, 8326 (2023).
49. Wang, S. et al. Temperature-dependent interphase formation and Li⁺ transport in Li metal batteries. *Nat. Commun.* **14**, 4474 (2023).
50. Feng, Y. et al. Enhancing microdomain consistency in polymer electrolytes towards sustainable Li batteries. *Angew. Chem. Int. Ed.* **64**, e202417105 (2025).
51. Liu, Y. et al. Regulating the solvation structure in polymer electrolytes for high-voltage Li metal batteries. *Angew. Chem. Int. Ed.* **63**, e202405802 (2024).
52. Hobold, G. M., Kim, K.-H. & Gallant, B. M. Beneficial vs. inhibiting passivation by the native Li solid electrolyte interphase revealed by electrochemical Li⁺ exchange. *Energy Environ. Sci.* **16**, 2247–2261 (2023).

53. Rong, Z. et al. How the PEG terminals affect the electrochemical properties of polymer electrolytes in Li metal batteries. *Energy Storage Mater.* **63**, 103066 (2023).
54. Li, Z. et al. Non-polar ether-based electrolyte solutions for stable high-voltage non-aqueous Li metal batteries. *Nat. Commun.* **14**, 868 (2023).
55. Xu, Y. et al. Direct in situ measurements of electrical properties of solid–electrolyte interphase on Li metal anodes. *Nat. Energy* **8**, 1345–1354 (2023).
56. Tan, Y.-H. et al. Inorganic composition modulation of solid electrolyte interphase for fast charging Li metal batteries. *Adv. Mater.* **36**, 2404815 (2024).
57. Zhang, Y. et al. Synergetic regulation of SEI mechanics and crystallographic orientation for stable Li metal pouch cells. *Nat. Commun.* **15**, 4454 (2024).
58. Gao, Q. et al. Superior Li-metal all-solid-state batteries with in-situ formed Li_3N -LiF-rich interphase. *Energy Storage Mater.* **63**, 103007 (2023).
59. Wang, S. et al. Preferentially oriented Ag-TiO₂ nanotube array film: an efficient visible-light-driven photocatalyst. *J. Hazard. Mater.* **399**, 123016 (2020).
60. Sun, Z. et al. Directing (110) oriented Li deposition through high-flux solid electrolyte interphase for dendrite-free Li metal batteries. *Angew. Chem. Int. Ed.* **62**, e202309622 (2023).
61. Ji, X. et al. Solid-state electrolyte design for Li dendrite suppression. *Adv. Mater.* **32**, 2002741 (2020).
62. Cao, W., Li, Q., Yu, X. & Li, H. Controlling Li deposition below the interface. *eScience* **2**, 47–78 (2022).
63. Feng, Y. et al. Production of high-energy 6-Ah-level Li || LiNi_{0.83}Co_{0.11}Mn_{0.06}O₂ multi-layer pouch cells via negative electrode protective layer coating strategy. *Nat. Commun.* **14**, 3639 (2023).
64. An, X. et al. Dielectric filler-induced hybrid interphase enabling robust solid-state Li metal batteries at high areal capacity. *Adv. Mater.* **36**, 2311195 (2024).
65. Chen, G. et al. A highly-fluorinated Li borate main salt empowering stable Li metal batteries. *Angew. Chem. Int. Ed.* **63**, e202400797 (2024).
66. Zhang, Y. et al. Rational molecular engineering via electron reconfiguration toward robust dual-electrode/electrolyte interphases for high-performance Li metal batteries. *ACS Nano* **18**, 14764–14778 (2024).

Acknowledgements

The authors are grateful for the support from the National Natural Science Foundation of China (No. 52473216), Shenzhen Science and Technology Major Project (KJZD20231023095359001) and Shenzhen Science and Technology Program (JCYJ20210324095412035, 20220808121346001), the Program for Guangdong Introducing Innovative and Entrepreneurial Teams (2019ZT08C642), Guangdong Basic and Applied Basic Research Foundation (2023A1515010045), the Project

of Department of Education of Guangdong Province (2024KTSCX059) and sponsored by CNPC Innovation Fund (2022DQ02-0401).

Author contributions

L.T. conceived the research idea and participated in manuscript revision and writing with input from all authors. W.J.X. designed the experimental plan, conducted the design, synthesis, and performance testing of electrolytes and electrodes, and wrote the manuscript. L.X.Z. participated in the writing and revision of the manuscript. S.X.L. performed density functional theory (DFT) calculations. J.H.H. carried out X-ray photoelectron spectroscopy (XPS) studies. Y.B.X. contributed to the preparation of electrolytes.

Competing interests

The authors declare no competing interests.

Additional information

Supplementary information The online version contains supplementary material available at <https://doi.org/10.1038/s41467-025-64345-7>.

Correspondence and requests for materials should be addressed to Lei Tian.

Peer review information *Nature Communications* thanks Rungroj Chanajaree and the other, anonymous, reviewer(s) for their contribution to the peer review of this work. [A peer review file is available].

Reprints and permissions information is available at <http://www.nature.com/reprints>

Publisher's note Springer Nature remains neutral with regard to jurisdictional claims in published maps and institutional affiliations.

Open Access This article is licensed under a Creative Commons Attribution-NonCommercial-NoDerivatives 4.0 International License, which permits any non-commercial use, sharing, distribution and reproduction in any medium or format, as long as you give appropriate credit to the original author(s) and the source, provide a link to the Creative Commons licence, and indicate if you modified the licensed material. You do not have permission under this licence to share adapted material derived from this article or parts of it. The images or other third party material in this article are included in the article's Creative Commons licence, unless indicated otherwise in a credit line to the material. If material is not included in the article's Creative Commons licence and your intended use is not permitted by statutory regulation or exceeds the permitted use, you will need to obtain permission directly from the copyright holder. To view a copy of this licence, visit <http://creativecommons.org/licenses/by-nc-nd/4.0/>.

© The Author(s) 2025